PCCP

ROYAL SOCIETY OF CHEMISTRY

PAPER

View Article Online
View Journal | View Issue

Cite this: *Phys. Chem. Chem. Phys.*, 2024, **26**, 7335

Holey penta-hexagonal graphene: a promising anode material for Li-ion batteries†

Linguo Lu,[a] Raven Gallenstein,[b] Xinghui Liu,[cd] Yi Lin,[e] Shiru Lin*[b] and Zhongfang Chen*[f]

Received 18th December 2023,
Accepted 6th February 2024

DOI: 10.1039/d3cp06146a

rsc.li/pccp

Carbon allotropes are widely used as anode materials in Li batteries, with graphite being commercially successful. However, the limited capacity and cycling stability of graphite impede further advancement and hinder the development of electric vehicles. Herein, through density functional theory (DFT) computations and *ab initio* molecular dynamics (AIMD) simulations, we proposed holey penta-hexagonal graphene (HPhG) as a potential anode material, achieved through active site designing. Due to the internal electron accumulation from the π-bond, HPhG follows a single-layer adsorption mechanism on each side of the nanosheet, enabling a high theoretical capacity of 1094 mA h g^{-1} without the risk of vertical dendrite growth. HPhG also exhibits a low open circuit voltage of 0.29 V and a low ion migration barrier of 0.32 eV. Notably, during the charge/discharge process, the lattice only expands slightly by 1.1%, indicating excellent structural stability. This work provides valuable insights into anode material design and presents HPhG as a promising two-dimensional material for energy storage applications.

1. Introduction

Rechargeable Li-ion batteries (LIBs) are widely used in electric vehicles, meeting the surging requirement for clean and sustainable energy resources in recent years.[1,2] In the pursuit of enhancing the performance of LIBs, carbon allotropes have emerged as promising candidates for anode materials due to their abundant source and cost-effectiveness.[3,4] Notably, with excellent conductivity and cycling stability, graphite has become the dominant commercial anode material, but the limited capacity hinders its broader applications.[5,6] Integration of two-dimensional (2D) materials may further improve the performance of LIBs and thus have been explored as an important strategy in next-generation anode innovation.[7–10]

Graphene,[11] essentially a single layer of graphite, holds immense potential with an impressive theoretical capacity up to 744 mA h g^{-1}, since it follows a two-sided single-layer adsorption mechanism, instead of the staging intercalation reaction mechanism observed in graphite.[12–14] However, the weak van der Waals interactions between monolayers may cause undesirable agglomeration, resulting in rapid performance degradation and compromised cycle stability.

To mitigate the restacking issue, holey graphene and its derivatives have emerged as a promising solution, introducing a porous structure that serves multiple purposes.[15,16] Firstly, it effectively diminishes the weak interactions between neighboring layers, thus preventing agglomeration and maintaining structural integrity, and also provides additional cross-plane ion transport channels, facilitating a rapid charge/discharge process.[17–20] Secondly, the specific porous framework enables accommodation of the local volume variation during Li-ion intercalation/extraction, thereby enhancing cycling.[21] Great progress has been achieved in developing holey graphene-based anode materials for LIBs. In 2016, Alsharaeh *et al.* successfully synthesized holey reduced graphene oxides (HRGO) by utilizing an etching method involving Ag nanoparticles. This method yielded HRGO with specific porous structures, featuring pores ranging from 2 nm to 5 nm. The resulting material exhibited a remarkable capacity, reaching 2.5 times that of reduced graphene oxides, and demonstrated an impressive retention of 94.6% reversible capacity after 100 charging/discharging cycles.[22] To further improve the cycling

[a] *Department of Physics, University of Puerto Rico, Rio Piedras, San Juan, PR 00931, USA*
[b] *Division of Chemistry and Biochemistry, Texas Woman's University, Denton, TX 76204, USA. E-mail: slin6@twu.edu*
[c] *Centre for Integrated Nanostructure Physics (CINAP), Institute of Basic Science (IBS), 2066 Seoburo, Jangan-Gu, Suwon 16419, Republic of Korea*
[d] *Department of Chemistry, Sungkyunkwan University (SKKU), 2066 Seoburo, Jangan-Gu, Suwon 16419, Republic of Korea*
[e] *Advanced Materials and Processing Branch, NASA Langley Research Center, Hampton, Virginia 23681, USA*
[f] *Department of Chemistry, University of Puerto Rico, Rio Piedras, San Juan, PR 00931, USA. E-mail: zhongfang.chen1@upr.edu*

† Electronic supplementary information (ESI) available. See DOI: https://doi.org/10.1039/d3cp06146a

performance, Bulusheva *et al.* proposed that the presence of various decorated O-containing (O–X) groups within HRGO could potentially influence capacity fading.[23] However, despite these advancements, the achieved capacity (around 430 mA h g^{-1}) of holey graphene-based anode materials falls short when compared to the theoretical capacity of graphene, thus presenting a new challenge in the design of anode materials. Notably, by means of first principles computations, Yu showed that modifying graphene's vacancy defects with nitrogen can transform hole sites into additional Li adsorption sites, providing up to 124.5 mA h g^{-1} capacity per nitrogen decoration.[24] Other strategies have also been proposed to increase specific capacities, such as optimization of the synthesis process,[25] heteroatom doping modification,[26–28] and compositional integration with transitional metal oxides.[29,30]

Recently, penta-graphene has been proposed as a promising carbon allotrope for high-capacity LIB anodes. Penta-graphene was proposed theoretically in 2015 as a unique carbon allotrope composed entirely of carbon pentagon rings (C5), instead of the hexagon rings (C6) found in graphene.[31] This novel structure adopts a buckling multi-decker arrangement with both sp^3 and sp^2 hybridized carbon atoms. Due to the slightly distorted structure, the sp^3-hybridized C atoms would split the p_z orbitals of the sp^2-hybridized ones and partially localize the electrons, generating an attractive adsorption potential for Li atoms at the sp^2 sites. Recognizing this potential, Xiao *et al.* investigated the performance of penta-graphene as LIB anode materials, and found that the presence of abundant active sites and its lightweight nature contribute to a specific theoretical capacity of up to 1489 mA h g^{-1}, while the isotropic furrow paths of the surface facilitate rapid metal ion diffusion.[32] However, the sp^2 restructuring process, which occurs in a stepwise exothermic manner, reveals a transformation tendency from penta-graphene to graphene, thereby highlighting the synthesis challenges associated with penta-graphene.[33] Nevertheless, one theoretically derived synthesis route has been proposed, starting from the pentalene molecule and progressing to bispentalene and penta-graphene nanoribbons, offering a promising prospect for potential experimental production.[34]

Inspired by the dibenzocyclooctadiyne molecule first synthesized by Sondheimer and co-workers in 1974,[35] Liu *et al.* successfully synthesized a new 2D carbon allotrope, namely holey graphyne (HGY),[36] with a periodic structure. In dibenzocyclooctadiyne, two aromatic benzene rings are connected by two bent acetylenic linkages, resulting in a highly strained octagon ring (C8), and the antiaromatic paratropicity of the central C8 ring is considerably attenuated. In the case of HGY, the carbon framework consists of interlinked C_6 rings connected by C≡C bonds, forming a distinct pattern of C_6 rings alongside highly strained C_8 rings. The fusion of aromatic rings and antiaromatic rings in HGY effectively impedes non-planar deformations and the disruption of π interactions within the C_8 rings, leading to the stability improvement. This achievement not only introduced a fresh perspective on the design of 2D carbon allotropes, but also serves as an inspiration for exploring the application of this concept in the development of novel LIB anode materials.

Dibenzo[*a*,*e*]pentalene,[37] a molecule comprising one antiaromatic pentalene and two aromatic benzene rings, caught our attention. The two fused benzene rings mitigate the antiaromatic character of pentalene, and thus enhance the stability of the whole molecule. This principle inspired us to design holey penta-hexagonal graphene (HPhG), a planar 2D nanomaterial (Fig. 1). The benzene rings preserve the planarity of neighboring C_5 rings, maintaining their π-interactions and creating active sites for Li adsorption on the C_5 rings. It is highly possible that the electron characteristic transformation from antiaromaticity to aromaticity for the C_5 rings enables strong Li ion adsorption with a single-layer mechanism, preventing dendrite formation in anode applications.

Herein, we report a new carbon allotrope, HPhG, by DFT computations. We verify its stabilities by binding energies, phonon spectrum, and *ab initio* molecular dynamics (AIMD) simulations. Our findings confirm that the HPhG monolayer exhibits robust stability as a planar semiconductor with a direct bandgap of 0.58 eV. Furthermore, we have explored the feasibility and mechanisms of HPhG as an anode material. Our computations demonstrate its high theoretical capacity of 1094 mA h g^{-1}, moderate open circuit voltage of 0.29 V, and low ion diffusion barrier of 0.32 eV. Remarkably, the electronic conductivity of HPhG can be substantially enhanced upon Li ions adsorption, transforming it into a conductor. Moreover,

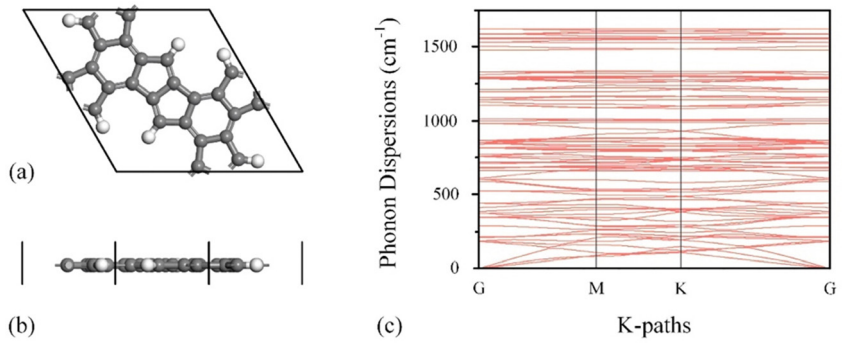

Fig. 1 Top (a) and side (b) views of the optimized unit cell of HPhG, where the gray and white atoms represent C and H atoms, respectively. (c) Phonon dispersion of HPhG. The carbon and hydrogen atoms are denoted by grey and white, respectively.

the charge/discharge events follow a single-layer adsorption mechanism, effectively preventing the formation of dendrites, which can help improve safety and cycle stability in practical applications. Our work not only introduces HPhG as a new 2D high-capacity anode material for LIBs, but also provides valuable insights into anode material design.

2. Computational methods

In our DFT computations, the CASTEP code[38] was employed for the majority of the computations, such as structure optimizations, thermodynamic and dynamic stability assessments of the material, and evaluation of HPhG's performance as LIB anode material, while the Vienna *ab initio* simulation package (VASP)[39] was used for calculating the band structure of HPhG monolayer and evaluating its thermal stability.

The electron exchange–correlation function was treated using the generalized gradient approximation (GGA), specifically the Perdew, Burke, and Ernzerhof (PBE) functional,[40] and the ultrasoft pseudopotentials were used to describe the ion-electron interactions.[41] The energy cutoff was set to 500 eV, and the convergence tolerance was 10^{-5} eV per atom. The Grimme's DFT-D method was employed to describe the van der Waals interactions,[42] and the zero-point energy was neglected due to the marginal effect on the Li adsorption.[43] To avoid spurious interactions between adjacent layers, a vacuum space of more than 15 Å was implemented in our computations. The Monkhorst–Pack k points were set as $8 \times 8 \times 1$ for geometry optimization and self-consistent calculations to achieve precision requirements in actual spacing (at least 0.015 1 $Å^{-1}$). We carried out both spin-polarized and spin-unpolarized computations and ensured the non-magnetic nature of HPhG monolayer.

Since the PBE functional typically underestimates the band gap in semiconductors and insulators, we employed the Heyd–Scuseria–Ernzerhof (HSE06) hybrid functional,[44,45] which is known to provide a more accurate estimation of the band gap in many materials, to calculate the band structure of HPhG. We also performed AIMD simulations to evaluate the thermal stabilities. During AIMD simulations, the PBE functional and the canonical ensemble (NVT) with a Nose–Hoover thermo stat[46–48] were employed, and a $2 \times 1 \times 1$ supercell was annealed at various temperatures. Each AIMD simulation was carried out for 10 ps with a time step of 1.0 fs.

3. Results and discussion

3.1. Structures, stability, and electronic properties

The HPhG monolayer exhibits a unique planar and porous structure, characterized by pore openings with a diameter of 5.31 Å. Its fundamental unit cell consists of 24 carbon atoms and six hydrogen atoms. As shown in Fig. 1a and b, among the carbon atoms in the five-membered rings (denoted as C5 atoms), the one at the pore edge shares a single C–C bond with its neighboring atom and is saturated by a hydrogen atom, similar to the antiaromatic molecular pentalene combining sp^2- and sp^3-hybridization. Notably, the carbon atoms in the six-membered rings (denoted as C6 atoms) in HPhG have two distinct bond types, with bond lengths of 1.38 Å and 1.46 Å, respectively. On the other hand, the C5 atoms display a range of bond lengths, varying between 1.38 Å and 1.44–1.48 Å. Compared with the antiaromatic pentalene (with bond lengths of 1.36 Å and 1.46–1.49 Å),[49] the bond lengths in the C5 rings of the HPhG monolayer are more equalized, indicating its increased aromaticity, thus increasing the stability of the whole HPhG system.

To investigate the stability of HPhG, we first evaluated its cohesive energies *via* the formula:

$$E_{coh} = (E_{HPhG} - n_C E_C - n_H E_H)/(n_C + n_H)$$

where E_C/E_H and E_{HPhG} are the total energies of a single C/H atom and HPhG, while the n_C and n_H present the number of C and H atoms per unit cell, which are 24 and 6, respectively. According to this definition, a more negative value of E_{coh} indicates that the material synthesis process is thermodynamically more favorable or energetically easier. The cohesive energy of HPhG, calculated to be −7.01 eV per atom, is lower than several experimentally synthesized carbon allotropes, such as T-carbon (−6.57 eV)[50] and α-graphyne (−6.93 eV).[51] It is also lower than the cohesive energies of recently predicted carbon materials, supertetrahedraphene (−6.43 eV)[52] and hexatetracarbon (−6.86 eV).[53] Furthermore, the E_{coh} value of HPhG is comparable to various 2D anode materials, *e.g.* penta-graphene (−7.08 eV),[54] graphdiyne (−7.20 eV),[55] γ-graphyne (−7.21 eV),[51] holey-graphyne (−7.30 eV),[36] and pop-graphene (−7.69 eV).[56] The low cohesive energy of HPhG is derived from the stabilization of connected C6 rings (causing partial sp^2 hybridization in C5s and tendency towards aromaticity), which suggests there is a viable route to engineering periodic structure with modification of intrinsic properties through molecular structure design, thus tuning the intrinsic properties of the material.

We then verified the dynamic stability of the HPhG monolayer by phonon dispersions. The absence of imaginary modes (Fig. 1c) in the first Brillouin zone confirms that it is dynamically stable. Given the importance of thermal stability as a critical metric for evaluating the performance across thermal ranges, as indicated in ref. 57, we further investigated this aspect through *ab initio* molecular dynamics (AIMD) simulations. These simulations were conducted over a duration of 10 ps at three distinct temperatures: 600 K, 800 K, and 1000 K, to comprehensively assess the material's thermal stability. HPhG monolayer maintained structural integrity with little ripples up to 1000 K (Fig. 2 and Fig. S1, ESI†). Note that the thermal stability of the HPhG monolayer is comparable to that of other related 2D materials. For instance, carbon allotropes like graphyne,[58] N/W doped BP monolayer,[59] and indium bismide,[60] also exhibit thermal stability at 1000 K. This similarity underscores the HPhG monolayer's significant temperature tolerance, reinforcing its suitability for advanced battery applications.

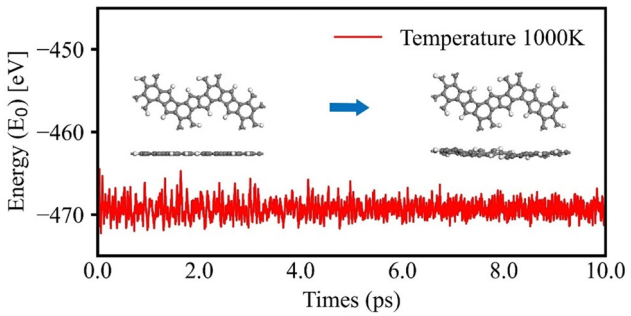

Fig. 2 Initial and final structures of HPhG, accompanied by the energy evolution diagram, following a 10 ps AIMD simulation at 1000 K. The carbon and hydrogen atoms are denoted by grey and white, respectively.

To study the electronic properties of HPhG, we calculated the band structure and Electron Localization Function (ELF) diagrams (shown in Fig. 3a and b). HPhG is a direct semiconductor with a narrow band gap of 0.58 eV (by HSE06 functional, 0.24 by PBE functional) as shown in Fig. 3a, which provides an acceptable conduction property. The ELF plot can be visualized as a contour plot in real space, displaying values ranging from 0 to 1. In this representation, a region with a value of 1 indicates perfect electron localization, suggesting the presence of localized electron pairs or strong covalent bonding. Conversely, a value of 0 signifies a region with low electron density, while a value of 0.5 implies the probability of a free electron-gas state. In the ELF plot, the presence of diffused low electron density surrounding carbon rings indicates the formation of π bonds within the HPhG monolayer. Conversely, the relatively high electron localization highlights the residual antiaromaticity of the C5 rings, resulting in a strong affinity for Li ions. Therefore, the excellent thermodynamic, dynamic, and thermal stabilities, as well as electronic properties, strongly indicate its high synthetic feasibility and application as electrode material for LIBs.

3.2. Application as an anode in LIBs

We first examined the adsorption structures of a single Li atom to evaluate the different possible adsorption sites and calculated the adsorption energies by:

$$E_{ads} = E_{sub+nLi} - E_{sub+(n-1)Li} - E_{Li}$$

where $E_{sub+nLi}$ and E_{Li} are the total energy of the substrate after nLi adsorption events, and the energy of a single Li in the metal Li bulk structure.

Based on symmetry considerations, we categorized the 15 potential sites into four distinct types: (1) polyatomic ring center positions, including site A above the C5 ring and site B above the C6 ring; (2) the bridge site between two bonded carbon atoms (sites C–sites H); (3) the top side of carbon atoms (the site I–site M); (4) side positions around the hollow surface, as the site N in the center and side site O close to the edge. All the proposed adsorption sites (from A to O) are schematically shown in Fig. S2 (ESI†). Among these 15 possible adsorption sites, only sites A, B, and O are thermodynamically stable with negative adsorption energy, which are illustrated in Fig. 4a. Li atoms in the whole bridge and top sites are transferred into A and B sites after geometry optimizations, and the hollow center site N is thermodynamically unstable. These unstable structures will not be considered.

The calculated adsorption energy of Li at the A-, B-, and O-sites are −0.54, −0.53, and −0.40 eV, respectively. Since a more negative value of E_{ads} corresponds to a higher binding strength between Li and the adsorption site, the A site is the most favorable adsorption position to store Li atoms during the charging process.

Theoretical storage capacity (TSC) and open-circuit voltage (OCV) are crucial parameters for evaluating the performance of electrode materials in LIBs from the thermodynamic point of view. In our study, we estimated these parameters by taking into account the Li adsorption on both sides of HPhG. In this way, we can assess the potential capacity for storing Li ions and determine the OCV, providing valuable insights into the electrochemical performance of HPhG as an anode material for LIBs. The OCV is calculated by the equation below:

$$OCV = [E_{sub+n_1Li} - E_{sub+n_2Li} - (n_1 - n_2)E_{Li}]/(n_2 - n_1)e$$

Our calculations indicate that the adsorption of the first two layers of Li atoms (12 Li atoms, as depicted in Fig. 4b and c) is an exothermic process, characterized by negative adsorption

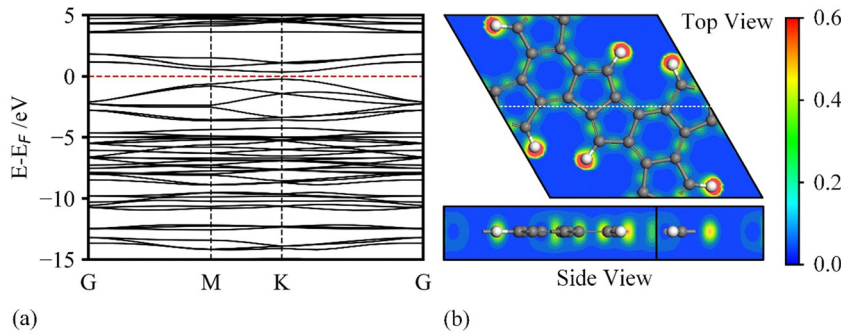

Fig. 3 (a) Band structure of holey penta-hexagonal graphene (HPhG) with 0.58 eV band gap (by HSE06 functional). (b) Electron location function of the unit cell. The white dotted line in the top view is the slice section for the side view. The carbon and hydrogen atoms are denoted by grey and white, respectively.

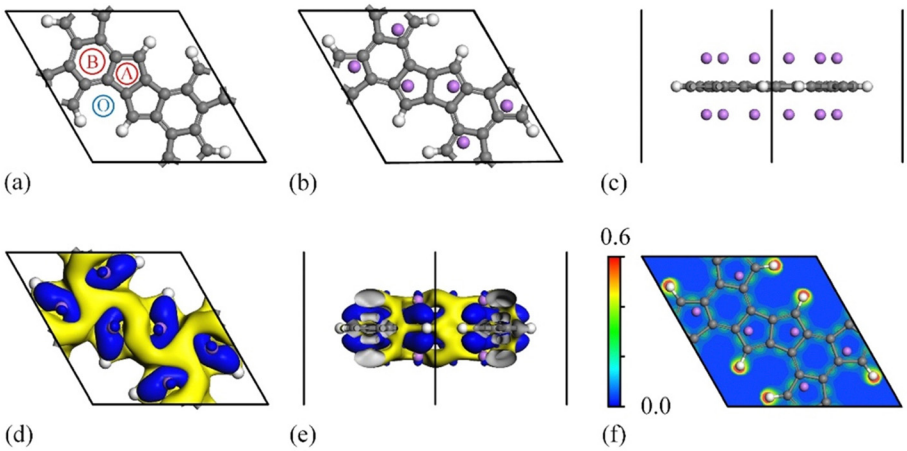

Fig. 4 (a) Three adsorption sites with negative adsorption energy. (b) Top view and (c) side view of the configuration after maximum adsorption. (d) Top view and (e) side view of the charge density differences after maximum adsorption. The cyan and yellow regions represent the charge accumulation and dissipation, respectively. (f) Top and side views of ELF plots of the HPhG with the maximum Li adsorption, where six Li atoms are adsorbed on each side. The carbon, hydrogen, and Lithium atoms are denoted by grey, white, and purple, respectively.

energy. On the other hand, the adsorption of the third layer of Li atoms is an endothermic process, meaning it is not favorable energetically. When the maximum concentration of Li atoms is used (with two layers of adsorbed Li atoms), the theoretical storage capacity approaches 1094 mA hg^{-1}, which is much higher than various carbon-based materials and 2D materials, as shown in Table 1. A higher OCV is beneficial for enhancing lithium storage capability but can hinder charge–discharge. To achieve rapid charge and discharge it is essential to maintain an optimal OCV range. Anodes generally prefer a low OCV, while cathodes perform better with a moderately high OCV. In the case of anode materials, typically retaining an OCV range of 0.1–1 V is ideal to prevent the formation of alkali metal dendrites during discharge/charge.[61] For the systems under consideration, the OCVs associated with one and two layers of adsorption are 0.35 V and 0.23 V, respectively, and the average OCV is 0.29 V, falling within the ideal potential range. Both the theoretical specific capacity (TSC) and the OCV values indicate that HPhG serves as a high-performance anode material for lithium-ion batteries.

Table 1 Theoretical storage capacity (mA h g^{-1}), diffusion barrier (eV), and open-circuit voltage (OCV, in V) of HPhG and some previously studied anode materials for LIBs

Materials	Capacity	Diffusion barrier	OCV	Ref.
C_2N	2939	0.80	0.45	62
Holey-graphite-46	1689	0.38	0.86	63
B-doped graphene	1564	0.24	0.37	64
Penta-graphene	1489	0.17	0.55	32
HfS_2	1378	0.13	2.37	65
Graphenylene	1116	0.25	0.46	66
HPhG	1049	0.32	0.29	This work
$C_6H_4O_2$-2D-MnO_2	588	0.28	2.21	67
Borophane	504	0.21	0.43	68
VS_2	466	0.22	0.93	69
Ti_3C_2	447.8	0.07	0.41	70
Phosphorene	433	0.76	1.63	71
ψ-graphene	372	0.31	0.01	72

To investigate the microscopic mechanism of Li adsorption, we conducted several analyses. First, we examined the charge density differences in the maximum adsorption structure (Fig. 4d and e), and found that electrons are accumulated between the Li atoms layer and carbon rings. Notably, there is a continuous charge distribution above the carbon rings (indicated by the blue color), forming a π-bond-like ring configuration, which enhances the delocalization of the charge spatial distribution. Then, we plotted the ELFs (Fig. 4f) to understand the adsorption behavior further. Compared with the ELF diagram before Li adsorption (in Fig. 3b), the HPhG with 12 Li atoms showed higher electron density at the π bond region and lower electron localization with dimmer spots. The feasible Li adsorption facilitated the transition of the C5 rings on the HPhG to a less localized state, which significantly improved the conductivity, transforming it from a semiconductor to a conductor (shown in Fig. S3, ESI†). The enhanced π-bonds preserved the maximum p orbital overlap, maintaining the characteristic planar structure. Furthermore, considering the adsorbed Li atoms, the electron cloud dissipation (the yellow part in Fig. 4d and e) and the absence of electron arrangement (in Fig. S4, ESI†) chemisorption appeared to exclusively occur between the adsorbates and the substrate, effectively preventing lateral dendrite growth between Li atoms. The lack of electron cloud arrangement also helped maintain the single-layer adsorption mechanism in HPhG and mitigates the risk of vertical dendrite growth. Moreover, there was no electron distribution outside the first Li atoms layer. It increased the transfer barrier of electron channels between the first Li layer and potential extra layers, which served to uphold the single-layer adsorption mechanism in HPhG and effectively prevented the formation of vertical dendrites.

The formation of Li clusters is undesirable and will affect cycle performance. After the adsorption on both sides, the nearest distance between two adsorbed Li atoms is 2.82 Å. It is larger than the bond length in Li_2 dimers (2.67 Å),[73] which

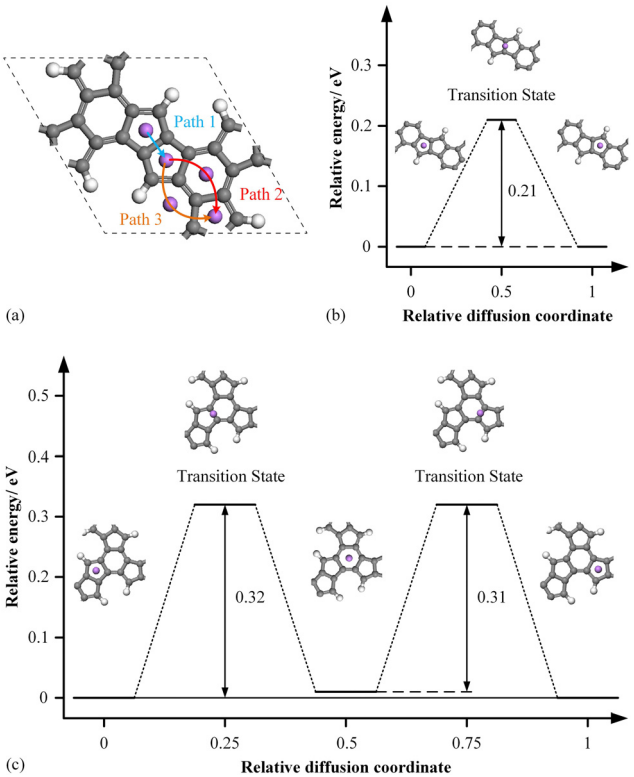

Fig. 5 (a) Three proposed ion transition pathways. (b) and (c) are the diagrams of transition structures and energy barriers. The carbon, hydrogen, and lithium atoms are denoted by grey, white, and purple, respectively.

further implies the prevention of Li clusters. From the adsorption and growth mechanism of Li storage mode, the one-layer adsorption mechanism on both sides of HPhG prevents disordered growth and avoids the Li vertical dendrite, which significantly improves its safety and feasibility in future applications. During the Li loading, the HPhG monolayer with 12 adsorbed Li atoms maintains its planar structure while the lattice constant expands slightly by 1.1%, indicating its high structural stability. Therefore, the anode material potential of HPhG shows a suitable capacity and good cycling stability.

To examine the Li transport kinetics of HPhG, we calculated the migration of Li atoms between adjacent A sites using the Linear Synchronous Transit/Quadratic Synchronous Transit (LST/QST) method.[74] From the perspective of the phase space, the stability of each geometry structure can be considered as one point in the energy surface, and the stable structures are at the local (B- and O-site) or global minimum (A-site). When a Li atom from one adsorption site transfers into a new one, it corresponds to the energy points' movement on the 3D surface. Typically, this transition occurs through a specific state known as the transition state. The presence of a transition state serves as a valuable means to assess the validity of proposed diffusion paths, providing an effective method for evaluating the accuracy of such pathways.

Thus, we examined three potential Li diffusion paths, as illustrated in Fig. 5a. Path-I involves the transfer of Li atoms between two interconnected A–A sites. In path-II, Li atoms move along the A–*B*–A sites on the surface, path-III entails crossing the surface hollow *via* A–O–A sites. However, there are no viable transition states identified between A- and O-sites, suggesting that path-III is unlikely. As shown in Fig. 5b and c, the computed diffusion barriers for path-I and path-II are 0.21 eV and 0.32 eV, respectively, with Path-II being the step that limits the overall rate of the diffusion process. The diffusion barrier of HPhG is lower than that of commercial graphite (0.4–0.6 eV) and compares favorably with various 2D electrode materials, as shown in Table 1. Moreover, the energy gap vanishes upon Li adsorption (Fig. S3, ESI†), resulting in a distinctive metallic characteristic and good electronic conductivity. Consequently, the combination of fast ion diffusion and exceptional electronic conductivity in HPhG further indicates its good performance as an anode material for LIBs.

4. Conclusion

By means of DFT computations and *ab initio* molecular dynamic simulations, we identified HPhG as a promising 2D holey carbon material for application as an anode material for LIBs. HPhG is thermodynamically, dynamically, and thermally stable. Moreover, upon Li adsorption, HPhG undergoes a semiconductor-to-conductor transformation, showing improved electrical conductivity. The low diffusion barrier (up to 0.32 eV) indicates the fast charge/discharge rate for LIBs. The maximum Li capacity reaches an impressive 1094 mA h g^{-1}, accompanied by a competitively low OCV of 0.29 V. By using charge density difference and ELF analyses, we have identified the single-layer adsorption mechanism and elucidated the reasons for the prevention of dendrite growth in HPhG. The concept of HPhG represents a remarkable exploration into harnessing the distinctive properties of pentalene and graphene-like structures. This investigation offers fundamental insights that can guide the design of future anode candidates through comprehensive bond analysis. With exceptional properties, we strongly believe that HPhG will emerge as a new platform for the development of high-performance anode materials for advanced lithium-based energy storage systems.

Conflicts of interest

There are no conflicts to declare.

Acknowledgements

This work was supported by the NSF Centre for the Advancement of Wearable Technologies (grant 1849243) and by NASA (grant number 80NSSC19M0236). S. L. acknowledges the startup fund from Texas Woman's University.

References

1 B. Dunn, H. Kamath and J.-M. Tarascon, *Science*, 2011, **334**, 928–935.

2 S. Chu, Y. Cui and N. Liu, *Nat. Mater.*, 2017, **16**, 16–22.
3 A. Rajkamal and R. Thapa, *Adv. Mater. Technol.*, 2019, **4**, 1900307.
4 M. M. Obeid and Q. Sun, *Carbon*, 2022, **188**, 95–103.
5 H.-H. Lee, C.-C. Wan and Y.-Y. Wang, *J. Power Sources*, 2003, **114**, 285–291.
6 K. Persson, Y. Hinuma, Y. S. Meng, A. Van der Ven and G. Ceder, *Phys. Rev. B: Condens. Matter Mater. Phys.*, 2010, **82**, 125416.
7 Y. Jing, Z. Zhou, C. R. Cabrera and Z. Chen, *J. Mater. Chem. A*, 2014, **2**, 12104–12122.
8 C. Zhang, A. Wang, J. Zhang, X. Guan, W. Tang and J. Luo, *Adv. Energy Mater.*, 2018, **8**, 1802833.
9 Z. Xiao, R. Wang, D. Jiang, Z. Qian, Y. Li, K. Yang, Y. Sun, Z. Zeng and F. Wu, *ACS Appl. Energy Mater.*, 2021, **4**, 7440–7461.
10 A. Hayat, M. Sohail, A. El Jery, K. M. Al-Zaydi, S. Raza, H. Ali, Z. Ajmal, A. Zada, T. A. Taha, I. U. Din, M. A. Khan, M. A. Amin, Y. Al-Hadeethi, A. Z. Barasheed, Y. Orooji, J. Khan and M. Z. Ansari, *Energy Storage Mater.*, 2023, **59**, 102780.
11 K. S. Novoselov, A. K. Geim, S. V. Morozov, D. Jiang, Y. Zhang, S. V. Dubonos, I. V. Grigorieva and A. A. Firsov, *Science*, 2004, **306**, 666–669.
12 G. Wang, X. Shen, J. Yao and J. Park, *Carbon*, 2009, **47**, 2049–2053.
13 Y. Liu, Y. M. Wang, B. I. Yakobson and B. C. Wood, *Phys. Rev. Lett.*, 2014, **113**, 028304–028308.
14 Y. Jing, Z. Zhou, C. R. Cabrera and Z. Chen, *J. Mater. Chem. A*, 2014, **2**, 12104–12122.
15 X. Han, M. R. Funk, F. Shen, Y. C. Chen, Y. Li, C. J. Campbell, J. Dai, X. Yang, J. W. Kim, Y. Liao, J. W. Connell, V. Barone, Z. Chen, Y. Lin and L. Hu, *ACS Nano*, 2014, **8**, 8255–8265.
16 Y. Lin, X. Han, C. J. Campbell, J. W. Kim, B. Zhao, W. Luo, J. Dai, L. Hu and J. W. Connell, *Adv. Funct. Mater.*, 2015, **25**, 2920–2927.
17 T. Liu, L. Zhang, B. Cheng, X. Hu and J. Yu, *Cell Rep. Phys. Sci.*, 2020, **1**, 100215.
18 A. C. Lokhande, I. A. Qattan, C. D. Lokhande and S. P. Patole, *J. Mater. Chem. A*, 2020, **8**, 918–977.
19 Y. Lin, Y. Liao, Z. Chen and J. W. Connell, *Mater. Res. Lett.*, 2017, **5**, 209–234.
20 Z. Jiang, B. Pei and A. Manthiram, *J. Mater. Chem. A*, 2013, **1**, 7775–7781.
21 J. Xu, Y. Lin, J. W. Connell and L. Dai, *Small*, 2015, **11**, 6179–6185.
22 E. Alsharaeh, F. Ahmed, Y. Aldawsari, M. Khasawneh, H. Abuhimd and M. Alshahrani, *Sci. Rep.*, 2016, **6**, 29854–29866.
23 L. G. Bulusheva, S. G. Stolyarova, A. L. Chuvilin, Y. V. Shubin, I. P. Asanov, A. M. Sorokin, M. S. Mel'Gunov, S. Zhang, Y. Dong, X. Chen, H. Song and A. V. Okotrub, *Nanotechnol.*, 2018, **29**, 134001.
24 Y. X. Yu, *Phys. Chem. Chem. Phys.*, 2013, **15**, 16819–16827.
25 Y. Lin, C. O. Plaza-Rivera, L. Hu and J. W. Connell, *Acc. Chem. Res.*, 2022, **55**, 3020–3031.
26 X. Wang, L. Lv, Z. Cheng, J. Gao, L. Dong, C. Hu and L. Qu, *Adv. Energy Mater.*, 2016, **6**, 1502100.
27 D. Wu, Y. Niu, C. Wang, H. Wu, Q. Li, Z. Chen, B. Xu, H. Li and L. Y. Zhang, *J. Colloid Interface Sci.*, 2019, **552**, 633–638.
28 R. Zhang, Y. Hou, X. Guo, X. Li, W. Li, X. Tao and Y. Huang, *Phys. Chem. Chem. Phys.*, 2023, **26**, 455–462.
29 C. Zhu, Z. Hui, H. Pan, S. Zhu, Q. Zhang, J. Mao, Z. Guo, Y. Li, M. Imtiaz and Z. Chen, *J. Mater. Chem. A*, 2019, **7**, 4788–4796.
30 D. Wu, W. Zhao, H. Wu, Z. Chen, H. Li and L. Y. Zhang, *Scr. Mater.*, 2020, **178**, 187–192.
31 S. Zhang, J. Zhou, Q. Wang, X. Chen, Y. Kawazoe and P. Jena, *Proc. Natl. Acad. Sci. U. S. A.*, 2015, **112**, 2372–2377.
32 B. Xiao, Y. Li, X. Yu and J. Cheng, *ACS Appl. Mater. Interfaces*, 2016, **8**, 35342–35352.
33 C. P. Ewels, X. Rocquefelte, H. W. Kroto, M. J. Rayson, P. R. Briddon and M. I. Heggie, *Proc. Natl. Acad. Sci. U. S. A.*, 2015, **112**, 15609–15612.
34 S. Li, Y. Shen, D. Ni and Q. Wang, *J. Mater. Chem. A*, 2021, **9**, 23214–23222.
35 H. N. C. Wong, P. J. Garratt and F. Sondheimer, *J. Am. Chem. Soc.*, 1974, **96**, 5604–5605.
36 X. Liu, S. M. Cho, S. Lin, Z. Chen, W. Choi, Y.-M. Kim, E. Yun, E. H. Baek, D. H. Ryu and H. Lee, *Matter*, 2022, **5**, 1–13.
37 M. Saito, M. Nakamura, T. Tajima and M. Yoshioka, *Angew. Chem., Int. Ed.*, 2007, **46**, 1504–1507.
38 M. C. Payne, M. P. Teter, D. C. Allan, T. A. Arias and J. D. Joannopoulos, *Rev. Mod. Phys.*, 1992, **64**, 1045–1097.
39 G. Kresse and J. Furthmü, *Phys. Rev. B: Condens. Matter Mater. Phys.*, 1996, **54**, 11169–11186.
40 J. Perdew, K. Burke and M. Ernzerhof, *Phys. Rev. Lett.*, 1996, **77**, 3865–3868.
41 J. M. Smith, S. P. Jones and L. D. White, *Phys. Rev. B: Condens. Matter Mater. Phys.*, 1990, **41**, 7892–7895.
42 S. Grimme, J. Antony, S. Ehrlich and H. Krieg, *J. Chem. Phys.*, 2010, **132**, 154104.
43 Y. X. Yu, *Phys. Chem. Chem. Phys.*, 2024, **26**, 323–335.
44 J. Heyd, G. E. Scuseria and M. Ernzerhof, *J. Chem. Phys.*, 2003, **118**, 8207–8215.
45 J. Paier, M. Marsman, K. Hummer, G. Kresse, I. C. Gerber and J. G. Angyán, *J. Chem. Phys.*, 2006, **124**, 154709.
46 W. G. Hoover, *Phys. Rev. A*, 1985, **31**, 1695–1697.
47 S. Nose, *Prog. Theor. Phys. Suppl.*, 1991, **103**, 1–46.
48 S. Nosé, *J. Chem. Phys.*, 1984, **81**, 511–519.
49 T. Bally, S. Chai, M. Neuenschwander and Z. Zhu, *J. Am. Chem. Soc.*, 1997, **119**, 1869–1875.
50 X.-L. Sheng, Q.-B. Yan, F. Ye, Q.-R. Zheng and G. Su, *Phys. Rev. Lett.*, 2011, **106**, 155703.
51 A. R. Puigdollers, G. Alonso and P. Gamallo, *Carbon*, 2016, **96**, 879–887.
52 Y. Yuan, J. Ma, S. Wu, J. Y. Lee and B. Kang, *Chem. Phys.*, 2021, **548**, 111257.
53 M. Naseri, J. Jalilian, D. R. Salahub, M. P. Lourenço and G. Rezaei, *Computation*, 2022, **10**, 19–27.
54 M. Wang, Z. Zhang, Y. Gong, S. Zhou, J. Wang, Z. Wang, S. Wei, W. Guo and X. Lu, *Appl. Surf. Sci.*, 2020, **502**, 144067.

55 C. Liu, Z. Liu, X. Ye, P. Cheng and Y. Li, *RSC Adv.*, 2020, **10**, 35349–35355.
56 P. Álvarez-Zapatero, A. Herrero, A. Lebon, L. J. Gallego and A. Vega, *Int. J. Hydrogen Energy*, 2021, **46**, 15724–15737.
57 D. G. Sangiovanni, R. Faccio, G. K. Gueorguiev and A. Kakanakova-Georgieva, *Phys. Chem. Chem. Phys.*, 2022, **25**, 829–837.
58 D. Yang, R. Jia, X. Wang and S. Bai, *ACS Appl. Nano Mater.*, 2023, **6**, 16684–16693.
59 J. Wu, J. H. Li and Y. X. Yu, *ACS Appl. Mater. Interfaces*, 2021, **13**, 10026–10036.
60 C. Lundgren, A. Kakanakova-Georgieva and G. K. Gueorguiev, *Nanotechnol.*, 2022, **33**, 335706.
61 D. Çakir, C. Sevik, O. Gülseren and F. M. Peeters, *J. Mater. Chem. A*, 2016, **4**, 6029–6035.
62 D. Wu, B. Yang, H. Chen and E. Ruckenstein, *Energy Storage Mater.*, 2019, **16**, 574–580.
63 C. Yang, X. Zhang, J. Li, J. Ma, L. Xu, J. Yang, S. Liu, S. Fang, Y. Li, X. Sun, X. Yang, F. Pan, J. Lu and D. Yu, *Electrochim. Acta*, 2020, **346**, 136244.
64 X. Guo, Y. Hou, X. Chen, R. Zhang, W. Li, X. Tao and Y. Huang, *Phys. Chem. Chem. Phys.*, 2022, **24**, 21452–21460.
65 Y. Kadioglu and Phys Chem, *Chem. Phys.*, 2022, **25**, 1114–1122.
66 Y. X. Yu, *J. Mater. Chem. A*, 2013, **1**, 13559–13566.
67 J. H. Li, J. Wu and Y. X. Yu, *J. Phys. Chem. C*, 2021, **125**, 3725–3732.
68 N. K. Jena, R. B. Araujo, V. Shukla and R. Ahuja, *ACS Appl. Mater. Interfaces*, 2017, **9**, 16148–16158.
69 Y. Jing, Z. Zhou, C. R. Cabrera and Z. Chen, *J. Phys. Chem. C*, 2013, **117**, 25409–25413.
70 D. Er, J. Li, M. Naguib, Y. Gogotsi and V. B. Shenoy, *ACS Appl. Mater. Interfaces*, 2014, **6**, 11173–11179.
71 S. Zhao, W. Kang and J. Xue, *J. Mater. Chem. A*, 2014, **2**, 19046–19052.
72 X. Li, Q. Wang and P. Jena, *J. Phys. Chem. Lett.*, 2017, **8**, 3234–3241.
73 H. L. Xu, Z. R. Li, D. Wu, B. Q. Wang, Y. Li, F. L. Gu and Y. Aoki, *J. Am. Chem. Soc.*, 2007, **129**, 2967–2970.
74 N. Govind, M. Petersen, G. Fitzgerald, D. King-Smith and J. Andzelm, *Comput. Mater. Sci.*, 2003, **28**, 250–258.

